ENVIRONMENTAL Science & Technology

pubs.acs.org/est Article

Substantial Underestimation of Fine-Mode Aerosol Loading from Wildfires and Its Radiative Effects in Current Satellite-Based Retrievals over the United States

Published as part of Environmental Science & Technology special issue "Wildland Fires: Emissions, Chemistry, Contamination, Climate, and Human Health".

Xing Yan, Chen Zuo, Zhanqing Li,* Hans W. Chen, Yize Jiang, Qiao Wang, Guoqiang Wang, Kun Jia, Yinglan A, Ziyue Chen, and Jiayi Chen

Cite This: *Environ. Sci. Technol.* 2024, 58, 15661−15671 Read Online

ACCESS | Metrics & More | Article Recommendations | Supporting Information

ABSTRACT: Wildfires generate abundant smoke primarily composed of fine-mode aerosols. However, accurately measuring the fine-mode aerosol optical depth (fAOD) is highly uncertain in most existing satellite-based aerosol products. Deep learning offers promise for inferring fAOD, but little has been done using multiangle satellite data. We developed an innovative angle-dependent deep-learning model (ADLM) that accounts for angular diversity in dual-angle observations. The model captures aerosol properties observed from dual angles in the contiguous United States and explores the potential of Greenhouse gases Observing Satellite-2's (GOSAT-2) measurements to retrieve fAOD at a 460 m spatial resolution. The ADLM demonstrates a strong performance through rigorous validation against ground-based data, revealing small biases. By comparison, the official fAOD product from the Moderate Resolution Imaging Spectroradiometer (MODIS), the Visible Infrared Imaging Radiometer Suite (VIIRS), and the Multiangle Imaging Spectroradiometer (MISR) during wildfire events is underestimated by more than 40% over western USA. This leads to significant differences in estimates of aerosol radiative forcing (ARF) from wildfires. The ADLM shows more than 20% stronger ARF than the MODIS, VIIRS, and MISR estimates, highlighting a greater impact of wildfire fAOD on Earth's energy balance.

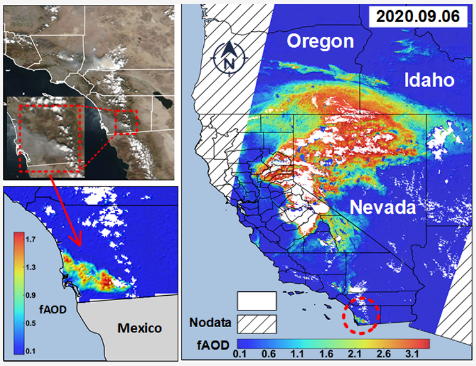

KEYWORDS: *GOSAT-2, fAOD, deep learning, wildfire, aerosol radiative forcing*

■ INTRODUCTION

Wildfires are a significant environmental concern, occurring globally and playing a significant role in the Earth's ecosystem.[1,2] While they have been a part of planet's geographical history, the frequency and intensity of wildfires have increased in recent years due to various factors such as climate change, land management, and human activities.[3,4] There have been significant increases in fire activities in the western United States (U.S.) in the past couple of decades.[2,5,6] While the particulate matter with diameters less than 2.5 μm ($PM_{2.5}$) has decreased dramatically across populated areas of the U.S., fine-mode aerosols chiefly from wildfires in the western U.S. have shown a reverse trend,[7] leading to increases in the contribution of smoke to total $PM_{2.5}$[8,9] and population exposure to unhealthy air.[10,11] Fine-mode aerosols profoundly influence Earth's radiation balance,[12] climate change,[13] and human health.[14] Accurately determining fine-mode aerosols from wildfire emissions is thus critical for assessing environmental and climate impacts.

The fine-mode aerosol optical depth (fAOD), a measure of fine-mode aerosol loading, is highly uncertain in most currently released satellite-based products, especially over land where most wildfires occur.[15] Many satellite instruments that retrieve fAOD are single-view-angle sensors, such as the Moderate-resolution Imaging Spectroradiometer (MODIS),[16,17] Advanced Himawari Imager (AHI),[18] and the Visible Infrared Imaging Radiometer Suite (VIIRS).[6,19] As a single-view algorithm, the accuracy of fAOD retrievals relies heavily on good knowledge of the surface reflectance.[20−22] However, accurately determining the surface reflectance over land is challenging due to complex surface properties and dynamic topographic variations.[23,24] This uncertainty raises concerns

Received: March 14, 2024
Revised: August 6, 2024
Accepted: August 7, 2024
Published: August 20, 2024

https://doi.org/10.1021/acs.est.4c02498

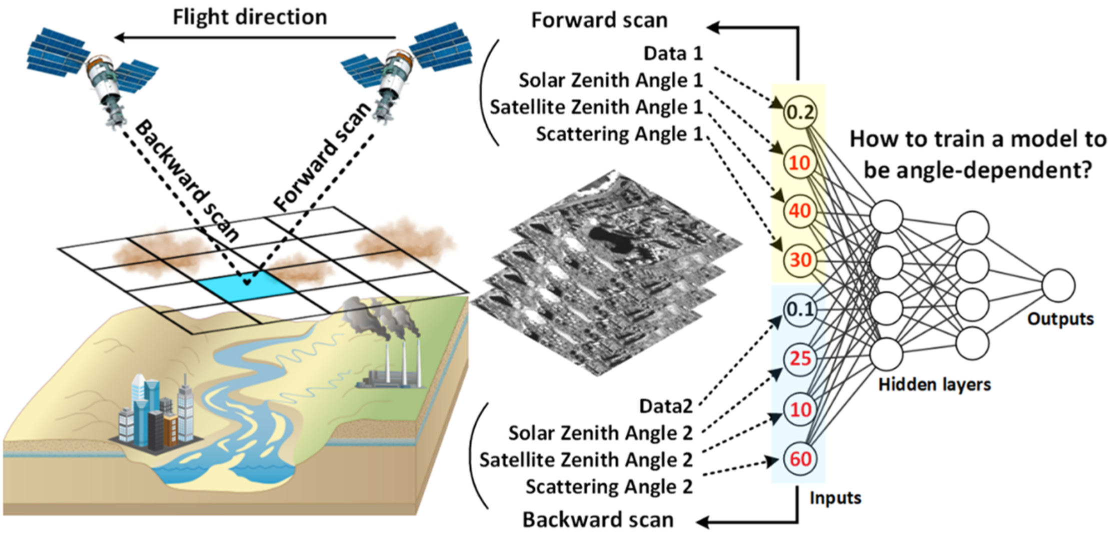

Figure 1. Deep neural networks still face challenges in modeling satellite data captured from different angles.

about a gap in our understanding of the overall fAOD burden resulting from wildfires.

As a new dual-angle Earth observation satellite, GOSAT-2 was launched on 29 October 2018.[25] One of its onboard sensors is the Thermal and Near-infrared Sensor for carbon Observation-Cloud and Aerosol Imager-2 (CAI-2), which measures reflected sunlight energy at the forward and backward scans. Previous studies have shown that dual-angle (AATSR)[26,27] and even multiangle (MISR)[28,29] satellite observations are much less dependent or independent of accurate surface reflectance and have a greater capacity to retrieve aerosol size information compared to single-view-based observations. However, most current aerosol retrieval schemes involve using look-up tables (LUTs) generated by radiative transfer models and may not encompass the full parameter space of real-world conditions.[30−33] As a result, LUT-based methods struggle to accurately retrieve aerosol properties outside their precomputed ranges,[34] leading to very large uncertainties in the retrieval of fAOD.

Deep learning has emerged as a powerful tool in recent years for satellite-based fAOD monitoring.[35−41] However, effectively utilizing the wealth of information contained in dual-angle measurements to enhance the retrieval of fAOD has not been exploited. GOSAT-2 provides near-simultaneous observations from two viewing angles. Therefore, a fundamental outstanding question is how to make a deep-learning model take advantage of these unique characteristics and train it to explicitly consider the varying angles, as illustrated in Figure 1.

To fill this research gap, we have developed a new angle-dependent deep learning model (ADLM) and applied it to quantify fAODs associated with wildfires in the western U.S. The new model can effectively leverage the angular information contained in GOSAT-2 measurements at a 460 m spatial resolution. The validation shows significant improvement upon current satellite-based estimates of wildfire-induced fAOD from which a better understanding of smoke aerosol radiative forcing can be gained.

MATERIALS AND METHODS

GOSAT-2 Data. GOSAT-2 is equipped with two advanced sensors: Fourier Transform Spectrometer-2 and CAI-2. Particularly notable are CAI-2's two bands in the ultraviolet region (339 and 377 nm), effective for characterizing aerosols over various landscapes, including urban areas. In addition to its proficiency in the shortwave infrared domain, CAI-2 has a high spatial resolution, i.e., 460 m. Tables S1 and S2 provide the specific parameters of CAI-2. In this study, we collected the CAI-2 data set for the contiguous United States from 2019 to 2022. Specifically, we resampled the shortwave infrared channel to 460 m, ensuring a consistent spatial resolution across other bands. For cloud masking, we employed the official cloud removal algorithm for the CAI-2 sensor, known as CLAUDIA 3 (more details about the algorithm in Section S2).[42,43]

MODIS and VIIRS fAOD. Both MODIS and VIIRS provide fine-mode fraction (FMF) data generated by the Dark Target algorithm from which fAOD is calculated as $\text{fAOD} = \text{AOD} \times \text{FMF}$.[44] We obtained Level 2-based fAOD from VIIRS (AERDT_L2_VIIRS_SNPP, spatial resolution of 6 km × 6 km) and MODIS (MYD04, Collection 6.1, spatial resolution of 3 km × 3 km), matching the GOSAT-2 time frame for the comparative validation analysis of fAOD at 550 nm (Table S3). It is worth noting that in the calculation of fAOD, we both apply quality control (QA = 3) to VIIRS or MODIS AOD to reduce uncertainties introduced by thin cirrus and smoke plumes.

MISR fAOD. The MISR onboard the National Aeronautics and Space Administration Earth Observing System Terra satellite has been successfully capturing global aerosol characteristics since 2000.[45] MISR possesses the capability to observe at nine different viewing angles, enabling it to quantify fine-mode aerosols, which are distinguished by their size of less than 0.35 μm in diameter (Table S3).[29] In this study, we employed the MIL2ASAE_3 product (level 2, version 3) for daily fAOD information at 550 nm of 4.4 km × 4.4 km.[46]

Ground-Truth fAOD Observations. AERONET[47] provides retrievals of aerosol properties around the world spanning more than 20 years, with a high temporal resolution of up to 15 min. To date, numerous studies have utilized this data set for characterizing and analyzing aerosol trends and validating satellite inversions.[15,48] In this study, to concurrently control the quality and quantity of data utilized by the model, since there are not enough level 2.0 data for use as training data for modeling purposes, here we selected Version 3.0,

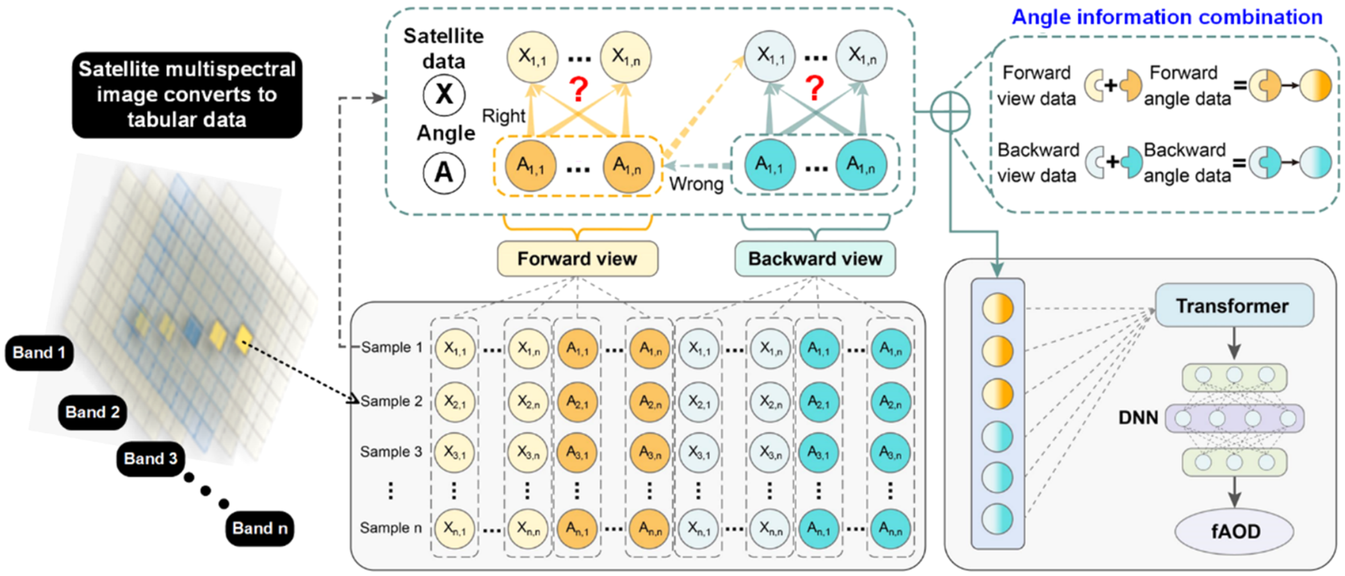

Figure 2. Overall architecture of the ADLM.

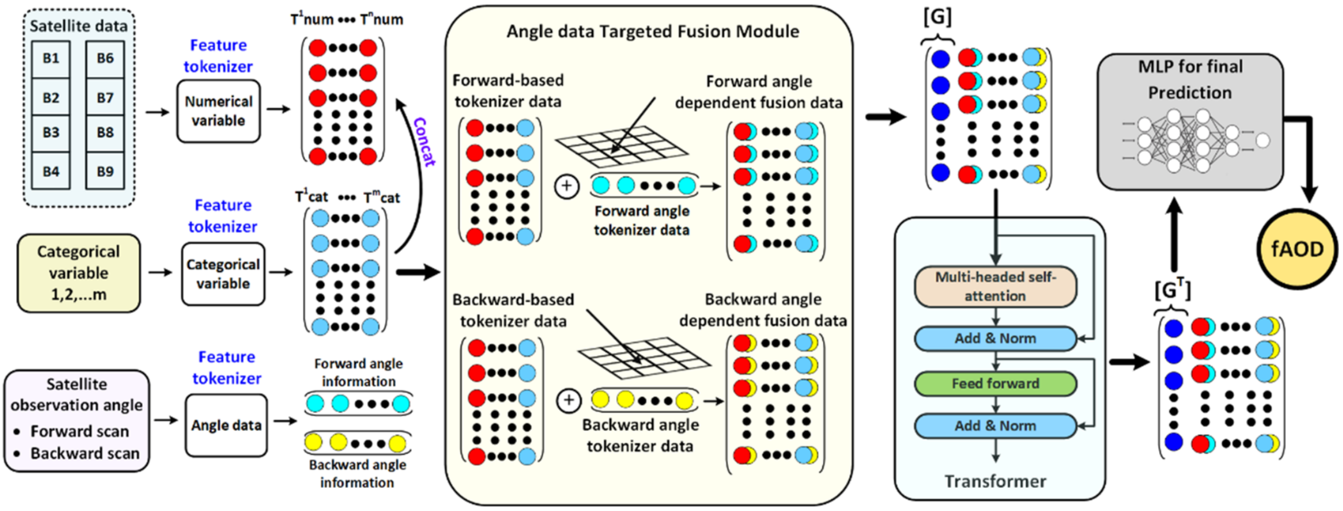

Figure 3. Schematic of the developed angle-dependent deep-learning model. MLP stands for the multilayer perceptron model.

spectral deconvolution algorithm (SDA) Level 1.5 (cloud-screened and quality controlled) fAOD data at 550 nm (interpolated using the Ångström exponent of fAOD, more details in Section S3), spanning 2019 to 2022 across the United States. AERONET sites are evenly distributed across the eastern and western parts of the United States (Figure S1a) and so can be fully utilized for model development and validation.

In addition, we also collected data from the SURFRAD network for independent model validation. SURFRAD has strategically established seven in situ measurement sites in climatologically diverse regions of the United States (Figure S1a and Table S4), providing AOD data at six wavelengths of the Multifilter Rotating Shadowband Radiometer (MFRSR).[49] Using the SDA algorithm, we calculated the SURFRAD fAOD at 550 nm. The validation and calibration of consistency between ground stations are crucial for fAOD verification.[50,51] Therefore, we selected nearby stations of the SURFRAD sites for accuracy comparison (Figure S1b,c). The results indicate good consistency (R:0.95) and similar trends of variation between the SURFRAD and AERONET sites, suitable for subsequent model validation (Figure S1d,e). It is worth noting that SURFRAD data was not used at any stage of the model's training process, ensuring the reliability of the model through independent validation.

FRAP. The FRAP (Fire and Resource Assessment Program) annually curates a detailed data set of fire perimeters in California. Representing the most comprehensive digital record in the state, FRAP provides precise boundaries with specific start and end times for each fire, moving beyond broader county-level data, making it suitable for our study.[52] To guarantee the reliability of the gathered data, FRAP was cross-referenced with multiple fire-reporting systems. Past studies often regarded FRAP as the standard product for evaluating and comparing wildfire-related data sets.[53,54] In our study, we employ the fAOD mean from within these FRAP boundaries to assess fire emissions.

ADLM. The newly developed ADLM for retrieving fAOD is capable of informing the model and training the data captured by imaging from two different angle GOSAT-2 signals (refer to Figure 2). We have created a module called "angle information combination" to combine GOSAT-2 angle information into the corresponding signal data. Generally, to establish a link between satellite signals and fAOD, it is necessary to transform images into a structured tabular format. Traditional models such as the Random Forest (RF) can handle this for single-angle satellite signals. However, when tabular data include signals from two different angles, RF cannot discern which data correspond to the first or second angles despite both angles observing the same physical feature. This limitation leads to a superficial understanding of the observational data, hindering the effective use of information obtained from the dual angles. The innovative ADLM demonstrates an ability to effectively address and resolve this pivotal challenge.

Figure 3 shows the detailed architecture of the ADLM. ADLM combines GOSAT-2 angle information into the corresponding observational data, then transforms all features (angle-dependent fusion data) to embeddings for transformer layers,[55] capturing dependencies. It is divided into four major steps. The first step involves processing the input data using the corresponding feature tokenizer method to prepare them for deep-learning computation. The second step utilizes the designed angle data targeted fusion module to combine the observed data with angle information. In the third step, the transformer technique is employed to integrate the combined data into the global feature [G]. Lastly, [G] is input into a multilayer perceptron (MLP) model for the inversion of fAOD.

First, the feature tokenizer is applied to three kinds of input data to embeddings T: numerical variables (GOSAT-2 measurements), categorical variables (month and season), and angle variables. This process is described as follows.

Feature tokenizer for numerical variables:

$$T^{n}_{\mathrm{num}} = x^{n}_{\mathrm{num}} \times w^{n}_{\mathrm{num}} + b^{n}_{\mathrm{num}} \tag{1}$$

where x^{n}_{num} is the nth numerical input, w^{n}_{num} is a real number ($\mathbb{R}$) vector $\mathbb{R}^{d}$, and b^{n}_{num} is the nth feature bias.

Feature tokenizer for categorical variables:

$$T^{m}_{\mathrm{cat}} = w^{m}_{\mathrm{cat}} \times e^{m}_{\mathrm{T}} + b^{m}_{\mathrm{cat}} \tag{2}$$

where e^{m}_{T} is a one-hot vector for the corresponding categorical feature.

The input numerical and categorical variables are transformed to embeddings:

$$T = \mathrm{Concat}[T^{n}_{\mathrm{num}}, \cdots T^{n}_{\mathrm{num}}, T^{1}_{\mathrm{cat}}, \cdots T^{m}_{\mathrm{cat}}] \in \mathbb{R}^{(n+m)\times d} \tag{3}$$

For the angle data tokenizer, we first designed sine- and cosine-based transform functions for GOSAT-2 forward and backward scan angles:

$$\begin{cases} V^{\mathrm{F}}_{\mathrm{Ang}} = \mathrm{Concat}[\sin(\alpha^{\mathrm{F}}), \sin(\beta^{\mathrm{F}}), \sin(\theta^{\mathrm{F}}), \cos(\alpha^{\mathrm{F}}) \\ \qquad , \cos(\beta^{\mathrm{F}}), \cos(\theta^{\mathrm{F}})] \in \mathbb{R}^{1\times 6} \\ V^{\mathrm{B}}_{\mathrm{Ang}} = \mathrm{Concat}[\sin(\alpha^{\mathrm{B}}), \sin(\beta^{\mathrm{B}}), \sin(\theta^{\mathrm{B}}), \cos(\alpha^{\mathrm{B}}) \\ \qquad , \cos(\beta^{\mathrm{B}}), \cos(\theta^{\mathrm{B}})] \in \mathbb{R}^{1\times 6} \end{cases} \tag{4}$$

where α is the satellite zenith angle, β is the solar zenith angle, θ is the scattering angle, and F and B are the forward and backward scans, respectively. The final feature tokenizer for angle data is

$$T^{i}_{\mathrm{Ang}} = V^{i}_{\mathrm{Ang}} \times w^{i}_{\mathrm{Ang}} + b^{i}_{\mathrm{Ang}},\ T^{i}_{\mathrm{Ang}} \in \mathbb{R}^{1\times d} \tag{5}$$

where $i \in [1, 2, \cdots, 6]$.

In the angle data targeted fusion module, a pointwise addition is conducted:

$$\begin{aligned} T_{\mathrm{Fus}} &= T \oplus T_{\mathrm{Ang}} \\ &= [(T^{1\times d}_{1} + T^{1\times d}_{\mathrm{Ang}}), (T^{1\times d}_{2} + T^{1\times d}_{\mathrm{Ang}})\cdots(T^{1\times d}_{n+m} + T^{1\times d}_{\mathrm{Ang}})] \\ &\in \mathbb{R}^{(n+m)\times d} \end{aligned} \tag{6}$$

A random real number matrix called the global feature $[G] \in \mathbb{R}^{1\times d}$ is then appended to

$$T_{0} = \mathrm{Concat}[[G], T_{\mathrm{Fus}}] \tag{7}$$

T_0 is then processed by the transformer layers:

$$T_{i} = F_{i}(T_{i-1}) \tag{8}$$

The final representation of $[G^{\mathrm{T}}]$[56] is used for calculating fAOD by a multilayer perceptron (MLP) model [each hidden layer has one fully connected (FC) layer, one dropout layer, and one rectified linear unit (ReLU) layer]:

$$\mathrm{fAOD} = \mathrm{linear}(\mathrm{dropout}(Relu([G^{T}]))) \tag{9}$$

For the model training, we used GOSAT-2 raw variable, derived variable (Table S5, more details in Section S4), and AERONET SDA fAOD (at 550 nm) as input data. The data set spanning four years (2019–2022) was randomly divided into training (70% of the data), validation (20% of the data), and testing (10% of the data) subsets. The validation data were instrumental in determining the model's hyperparameters. Table S6 outlines the final hyperparameter values for the ADLM. Leveraging well-trained models, we generated daily fAOD products for the years 2019 to 2022 at a spatial resolution of 460 m, subsequently subjecting them to evaluation against AERONET fAOD retrievals.

To conduct an independent validation, we employed fAODs obtained from SURFRAD sites (Figure S1 and Table S4). Note that the SURFRAD sites chosen for this validation were deliberately selected to be distinct from those utilized by AERONET and were not integrated into the modeling process. Consequently, fAODs from these SURFRAD sites were used exclusively for independent validation purposes. In addition, to assess the efficacy of the ADLM in inferring fAOD in regions devoid of ground-based measurement sites, we employed a rigorous approach known as site-based 5-fold cross-validation. In this method, we divided the AERONET sites into five subsets, each containing a distinct 20% of the available measurement sites. During each iteration of the cross-validation, one of these subsets was held out as a test set, while the remaining 80% were used for model training. This process was repeated five times, with each subset taking on the role of the test set once. This ensured a comprehensive evaluation of the model's performance and its ability to generalize to unseen locations.

Radiative Forcing of the fAOD Direct Effect. This study adopted the method developed by Nakajima et al.[57] for calculating clear-sky fine-mode aerosol radiative forcing ($\mathrm{ARF}^{\mathrm{fAOD}}$) at the top of the atmosphere ($\mathrm{ARF}^{\mathrm{fAOD}}_{\mathrm{TOA}}$), within the atmosphere ($\mathrm{ARF}^{\mathrm{fAOD}}_{\mathrm{ATM}}$), and at the surface ($\mathrm{ARF}^{\mathrm{fAOD}}_{\mathrm{SFC}}$):

$$\begin{aligned} \mathrm{ARF}^{\mathrm{fAOD}}_{\mathrm{SFC}} &= -(1 - A_{\mathrm{g}})(1 - \omega f)\tau TSD/R^{2}, \\ \mathrm{ARF}^{\mathrm{fAOD}}_{\mathrm{TOA}} &= -[\omega b - A_{\mathrm{g}}(1 - \omega f)]\tau TSD/R^{2}, \\ \mathrm{ARF}^{\mathrm{fAOD}}_{\mathrm{ATM}} &= \mathrm{ARF}^{\mathrm{fAOD}}_{\mathrm{TOA}} - \mathrm{ARF}^{\mathrm{fAOD}}_{\mathrm{SFC}} \end{aligned} \tag{10}$$

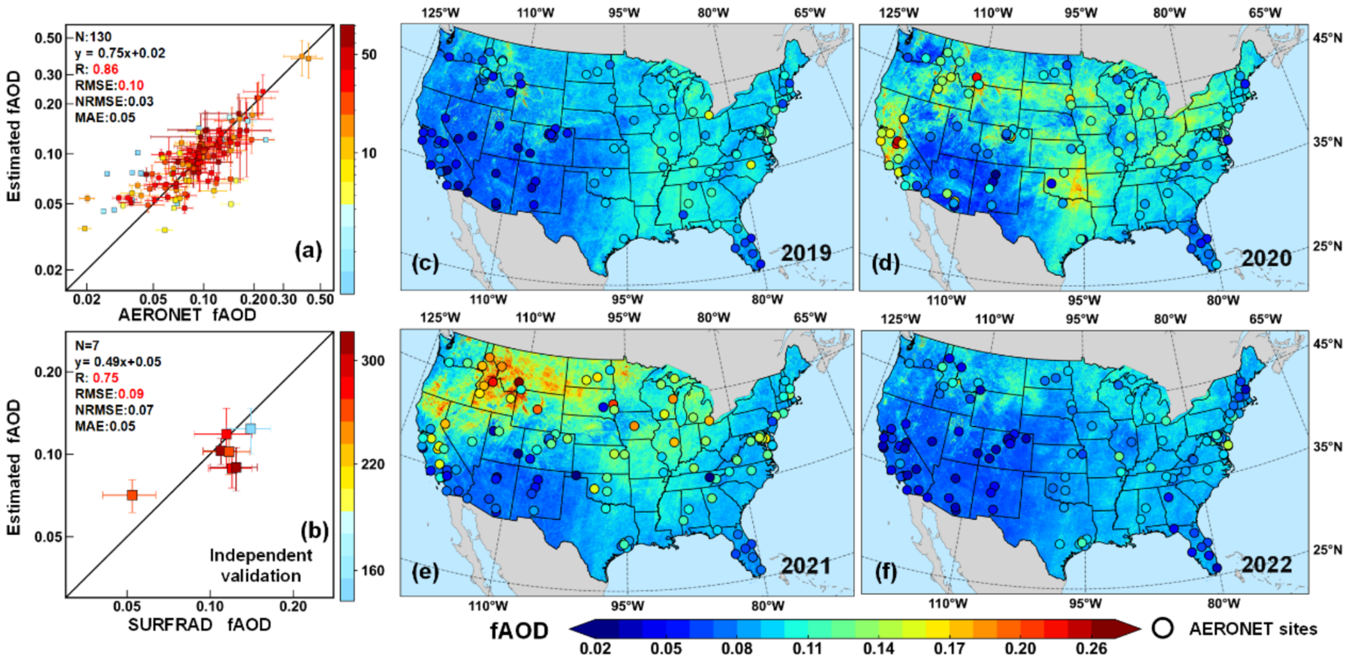

Figure 4. Validation and spatial view of ADLM fAOD. (a, b) Density scatterplots of fAOD derived from the ADLM against fAODs from AERONET and SRFRAD, respectively, in the contiguous U.S. for the years 2019−2022. Points and error bars represent means and standard deviations of the ADLM retrievals (vertical lines) and in situ measurements (horizontal lines). The number of samples (*N*), relation from linear regression, correlation coefficient (*R*), root-mean-square error (RMSE), normalized RMSE (NRMSE), and mean absolute error (MAE) are given in each panel. (c−f) Annual average ADLM fAODs across the contiguous U.S. for the period 2019−2022. Colored dots represent the annual mean AERONET fAODs.

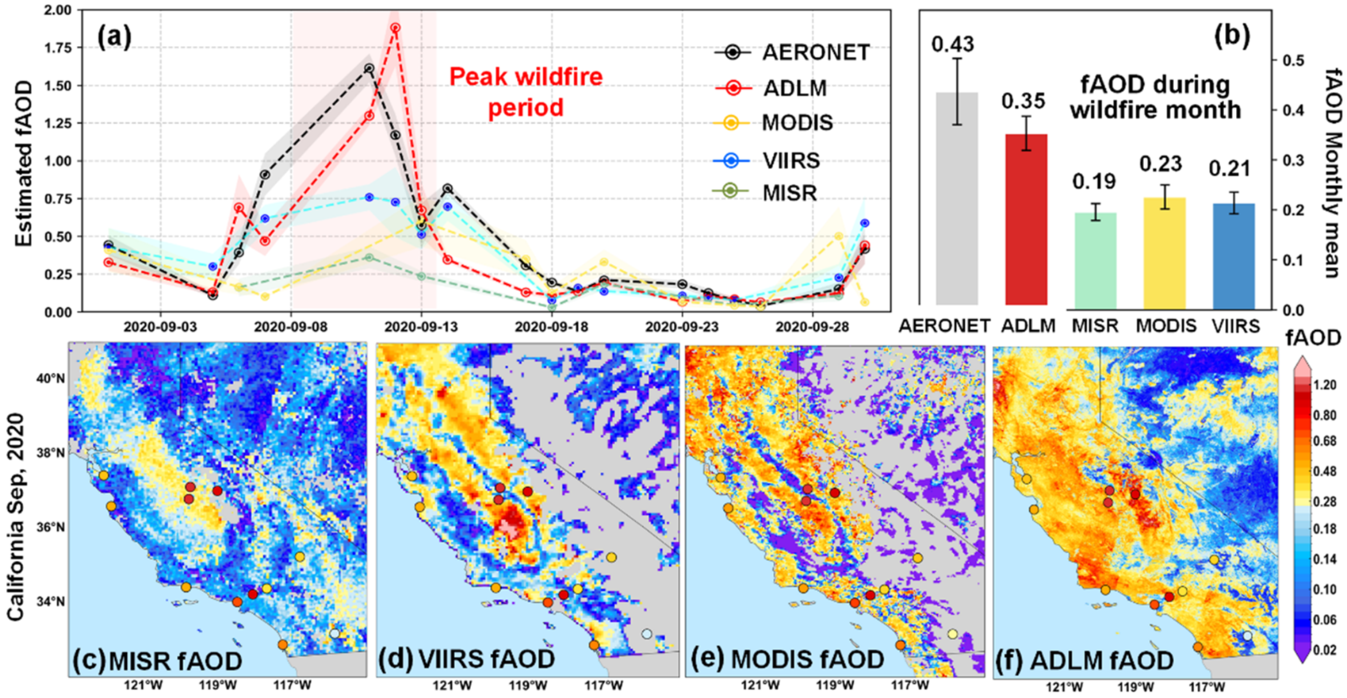

Figure 5. Satellite-based fAOD under fire conditions. (a) Daily mean fAOD obtained by AERONET (black), ADLM (red), MODIS (yellow), VIIRS (blue), and MISR (cyan) over California in September 2020. The wildfire-pr1 day in this month California is highlighted by the shadows.We. (b) Monthly mean fAOD for each product over California in September 2020. The black Error bars represent the standard deviation of monthly mean. (c−f) Spatial distributions of MISR-, VIIRS-, MODIS-, and ADLM-drieved-fAOD with ground-based observations in California, September 2020.

where A_g is the surface albedo from the MODIS albedo product (MCD43A1); *S* is the incident solar flux at the top of the atmosphere (1370 W/m^2); *D* is the daytime fraction of the day; *R* is the Earth−Sun distance in astronomical units; *g* and *ω* are the AERONET-retrieved asymmetry factor and aerosol single-scattering albedo, respectively; $f = (1 + g)/2$ and $b = (1$

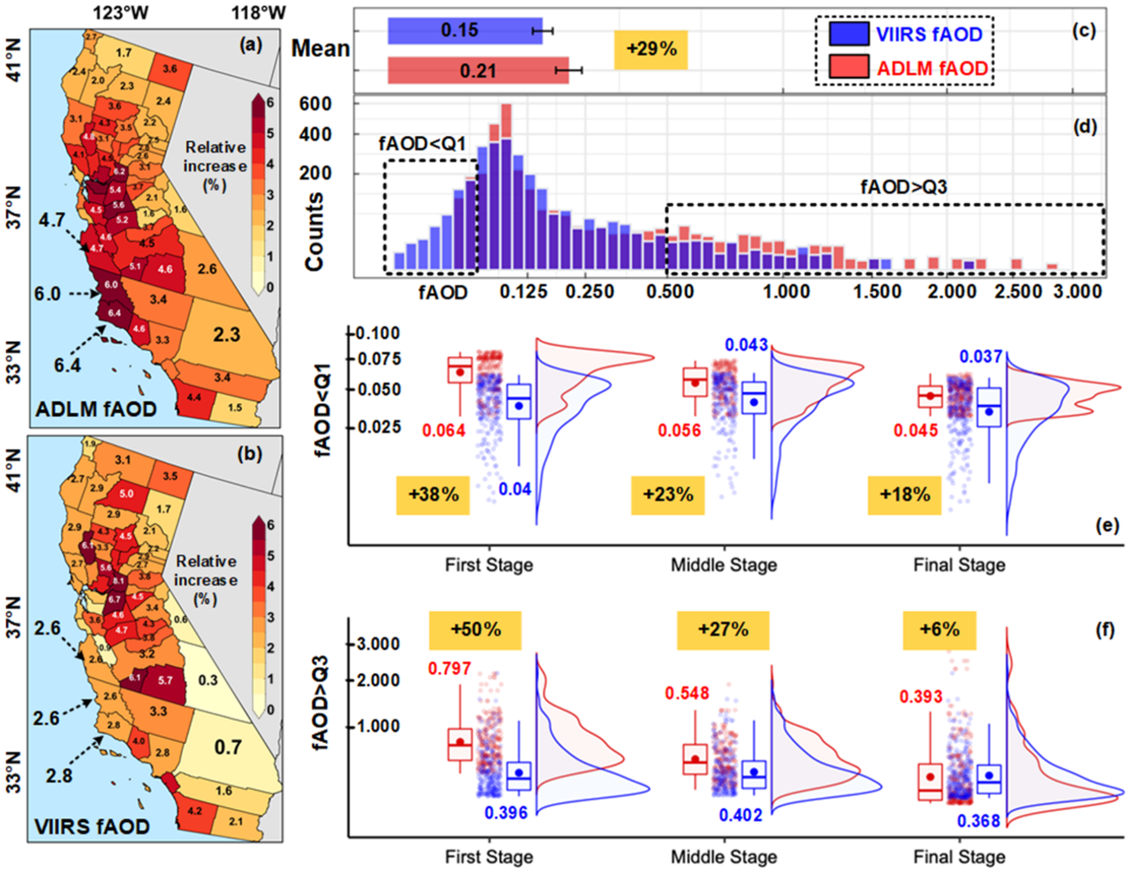

Figure 6. Relative change in fAOD between September 2020 (extreme wildfire period based on Fire and Resource Assessment Program (FRAP) data) and September 2019 (normal period) for (a) ADLM and (b) VIIRS. Mean (c) and histogram (d) of fAOD estimated by ADLM and VIIRS during wildfires. Comparison of ADLM and VIIRS fAODs (e) below the 25th percentile (Q1) and (f) above the 75th percentile (Q3) during three wildfire stages: (1) the first one-third of the entire wildfire period, (2) the middle stage of the next one-third, and (3) the final last one-third.

$- g)/2$; and T is the transmissivity of the atmosphere calculated here using the Second Simulation of a Satellite Signal in the Solar Spectrum radiative transfer model.

RESULTS

fAOD Derived by the ADLM from GOSAT-2 Measurements. Applying the ADLM to GOSAT-2 data, we calculated fAODs at a spatial resolution of 460 m across the contiguous United States from 2019 to 2022. Figure 4a,b shows comparisons of ADLM-modeled fAODs with Aerosol Robotic Network (AERONET)-retrieved (validation) and Surface Radiation Budget (SRFRAD)-retrieved (independent validation) fAODs, respectively. The validation with AERONET retrievals (Figure 4a) shows a correlation coefficient (R) of 0.86 and a root-mean-square error (RMSE) of 0.10, with over 64.17% of the data falling within the ± (0.03 + 10%) error envelope (EE; Figure S2). For the independent validation with SRFRAD retrievals (Figure 4b), R is 0.75 and the RMSE is 0.09, with 51.50% of the data falling within the EE (Figure S2). To assess the performance of the ADLM in areas devoid of ground-based stations, we conducted a more rigorous site-based 5-fold cross-validation. In each fold, 20% of the sites were excluded from model training, participating only in the final testing phase (Figure S3). Test results show that the R of the ADLM ranges from 0.81 to 0.85, while the RMSE ranges from 0.09 to 0.12. This indicates that ADLM has excellent stability and retrieval accuracies in regions without ground-based stations.

Compared to the conventional machine learning RF model and ADLM without angular fusion ($\text{ADLM}_{\text{no-angle-fusion}}$), the ADLM results show that R increased by 14 and 6% for RF and $\text{ADLM}_{\text{no-angle-fusion}}$, respectively, with RMSE decreasing by 23 and 17% (Figure S4). This results in a larger portion of data falling within the EE, improving by 15% relative to the RF model and by 8% relative to ADLMno-angle-fusion. For the RF model, this improvement is particularly pronounced in the inversion of low fAOD values (below the fourth quartile), with a substantial increase from 11 to 17% in data falling within the EE. Figure 4c−f shows the spatial distributions of annual mean modeled and AERONET-retrieved fAODs from 2019 to 2022, revealing a high degree of spatial consistency between them. Figure S5 demonstrates how the ADLM's 460 m spatial resolution accurately captures fAOD spatial details. This new data set offers valuable insights for environmental research, especially in identifying and characterizing fAOD emission sources. A standout example is the Marathon refinery in California, as shown in Figure S5, illustrating the benefits of this high-resolution fAOD data set. With its 460 m resolution, it allows for precise pinpointing of fAOD emissions from specific sources like the Marathon refinery.

Implications for Our Understanding of fAOD under Fire Conditions. Figure 5a shows ADLM-derived, MODIS-derived, VIIRS-derived, MISR-derived, and AERONET-retrieved daily fAODs in California in September 2020. To ensure consistency in comparisons, we used the temporal frequency of ADLM fAOD as the standard to match the other

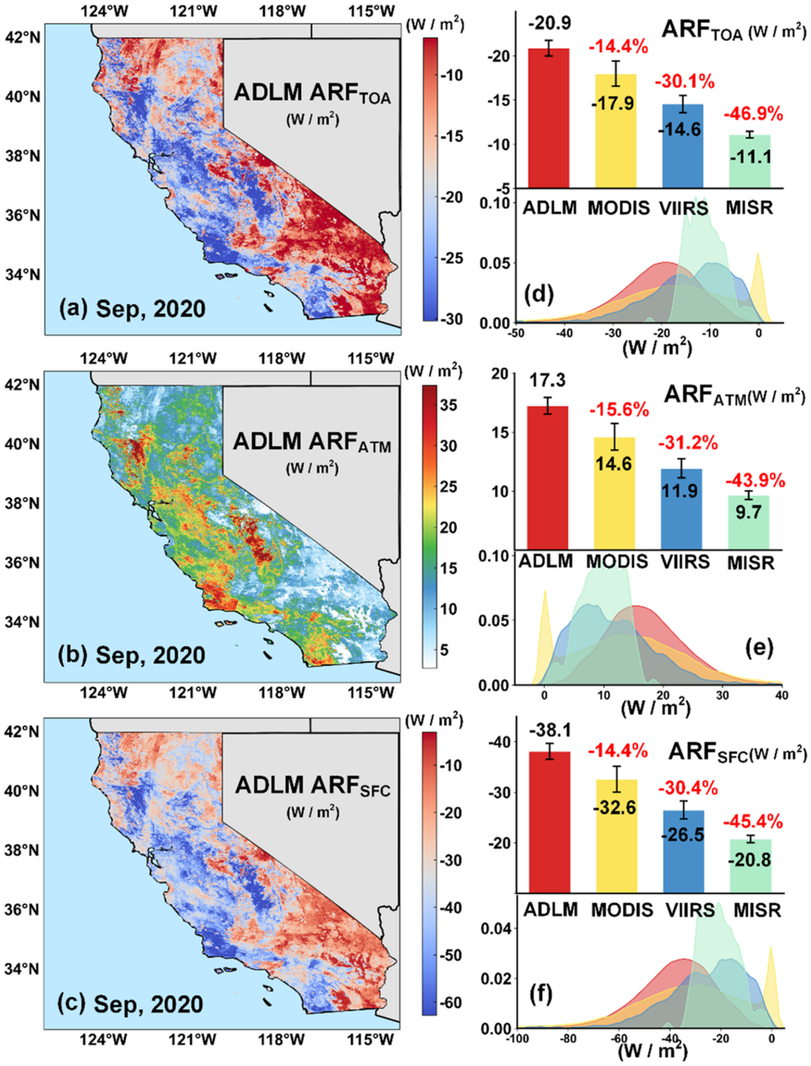

Figure 7. Spatial distributions of ADLM-based fAOD radiative forcing during the California wildfires in September 2020 at the top of the atmosphere (a), within the atmosphere (b), and at the surface (c). (d−f) Mean (top) and distribution density (bottom) of fAOD ARF$_{TOA}$, ARF$_{ATM}$, and ARF$_{SFC}$ estimated by ADLM, VIIRS, MODIS, and MISR during September 2020.

products, considering samples with spatial coverage greater than 50% as valid. In this month, California witnessed the largest wildfire recorded in the U.S., burning more than 1.2 million acres. AERONET shows that the average fAOD value reached ∼0.43 (Figure 5b). However, MODIS-derived, VIIRS-derived, and MISR-derived fAOD values were significantly less, with a monthly average value of 0.23, 0.21, and 0.19, respectively (47, 51, and 56% underestimation relative to the AERONET fAOD). On the intensely wildfire-affected day of September 11, 2020, the VIIRS-derived fAOD (0.75) was less than the AERONET fAOD (1.6) by 53% (Figure 5a). By contrast, the ADLM-derived fAOD (1.27) was much closer under wildfire conditions. In comparison with AERONET data, the Multiangle Imaging Spectroradiometer (MISR) demonstrated a good correlation (R = 0.69, Figure S6), consistent with previous research highlighting its multiangle observational capability and superior aerosol size estimation.[46,58] However, Figure 5a reveals that MISR tends to significant underestimation in situations with high fAOD. This underestimation is also corroborated by Figure S6, which reveals that a significant number of MISR fAOD values fall below the 1:1 line, indicating a severe undervaluation. These underestimation issues in the official fAOD products of the MODIS, VIIRS, and MISR arise not only because of the inherent limitations of the algorithms employed but also because of the spatial resolution, which is a contributing factor to the observed underestimation. To our knowledge, most official data sets produce fAOD products at kilometer-level or coarser spatial resolutions, such as MODIS's 3 km, VIIRS's 6 km, and MISR's 4.4 km fAOD data (Figure 5c−e). The use of coarse-resolution data sets in quantitative analyses may introduce a significant degree of uncertainty, particularly where small-scale wildfire sources remain challenging to detect.[59] The newly improved fAOD data set, offering a detailed 460 m resolution, more effectively illustrates the spatial distribution and detailed analysis of fAOD (Figure 5f). This advancement is clearly demonstrated in the cases of California and Montana, as shown in Figure S7. The monthly average results from these two regions exhibit noticeable cyclic fluctuations in fAOD values, with higher levels occurring during the summer, exceeding 0.2, and lower levels occurring during the winter, typically below 0.1. Especially during periods of intense wildfires, the monthly average fAOD values in California and Montana exceeded 0.3 and 0.4, respectively,

https://doi.org/10.1021/acs.est.4c02498

which represents a 3- to 4-fold increase compared to the same period, underscoring the significant impact of wildfires on atmospheric aerosol loading. Additionally, the data set's precision allows for the detection of smoke from active fires at specific locations, such as those illustrated in Figure S8, including the Silver Peak Wilderness and Cleveland National Forest. This enhanced capability facilitates the effective detection and monitoring of fAOD emissions, even from small-scale fire events.

The figure highlights the underestimation of VIIRS fAOD products compared to ADLM in California. We excluded MODIS fAOD from this comparison due to its lower accuracy compared to VIIRS fAOD in validation. Additionally, the MISR fAOD was not incorporated into the comparison because its temporal resolution of 9 days is not sufficient to discern fAOD variations across different wildfire periods.[46] For the whole regional scope of California, we chose two distinct periods, September 2019 and September 2020, representing normal and fire active years, respectively. The occurrence of wildfires led to significant surges in fAOD emissions in 2020, four to six times higher than that in a normal year like 2019, especially in California's coastal regions (Figure 6a). This is in contrast to the VIIRS product showing only a moderate rise (Figure 6b). Furthermore, we conducted a comparative analysis of fAOD values for each fire event during September 2020 in California by fire boundary data from the Fire and Resource Assessment Program (FRAP), specifically across various wildfire periods. Wildfires are equally segmented into three distinct stages throughout their lifecycle record by FRAP, which enables us to analyze how fAOD fluctuates from the initial ignition to the peak burning phase and finally to the decline in fire activity. Figure 6c shows that relative differences between VIIRS- and ADLM-based mean fAOD (|VIIRS fAOD − ADLM fAOD| ÷ ADLM × 100%) reach up to 29% (mean ADLM and VIIRS fAOD values equal to 0.21 and 0.15, respectively). Notably, VIIRS yields lower fAOD values at the lower 25th percentile (Q1). Conversely, for values exceeding the 75th percentile (Q3), the ADLM captures higher fAOD values. The underestimation in VIIRS fAOD retrievals is most pronounced during the first stages of wildfires, with high values (>Q3) underestimated by 50% and low values (<Q1) underestimated by 38% (Figure 6e,f). We employed FRAP data to examine the areal coverage of fire-affected areas in California from 2019 to 2022. As shown in Figure S9, the highest frequency of fires occurred in 2020 when the VIIRS fAOD was less than the ALDM fAOD by 78%, while the overall difference was 75% for the four years considered, suggesting that VIIRS may not be capturing the full extent of fAOD associated with these fires. This underestimation can have implications for pollution assessments and understanding of the climate impact of wildfires.

Figure 7a−c shows mean ADLM-derived fAOD direct radiative forcing at the top of the atmosphere (TOA), at the surface (SFC), and within the atmosphere (ATM) over California for September 2020. Due to a major contribution by wildfire emissions, average fAOD net radiative effects are negative (ADLM $\mathrm{ARF_{TOA}} = -20.9\ \mathrm{W/m^2}$, Figure 7 d), resulting in TOA cooling over California. There is also cooling at the surface, with mean ADLM $\mathrm{ARF_{SFC}} = -38.1\ \mathrm{W/m^2}$ (Figure 7e). By contrast, within the atmosphere, fAOD has a warming effect (mean ADLM $\mathrm{ARF_{ATM}} = 17.3\ \mathrm{W/m^2}$, Figure 7f), indicating an increase in radiative heating in the atmospheric column. When compared to the ADLM outcomes, the negative radiative effects obtained by MODIS, VIIRS, and MISR fAODs at the TOA are reduced by approximately 14.4, 30.1, and 46.9%, respectively. This relative underestimation of negative impacts is also evident in the $\mathrm{ARF_{SFC}}$ comparisons. Previous studies have reported a similar magnitude of $\mathrm{ARF_{SFC}}$ from biomass-burning aerosols as VIIRS, i.e., −15.9[60] to $-17.1\ \mathrm{W/m^2}$.[61] In a past study, Chemke et al.[62] demonstrated that direct aerosol radiative forcing influences local thermodynamic and dynamic changes by altering surface temperature, further regulating atmospheric circulation. This underestimation could exacerbate uncertainties in understanding climate change. Additionally, the warming effect in the atmosphere as observed through MODIS, VIIRS, and MISR fAODs is noticeably weaker than that detected with the ADLM fAOD, showing decreases of 15.6, 24.1, and 43.9% in their respective warming effects. From a spatial perspective, significant disparities in ARF between ADLM, MODIS (Figure S10), VIIRS (Figure S11), and MISR (Figure S12) are observed. Particularly in wildfire-affected regions, the MODIS, VIIRS, and MISR fAOD negative effect is markedly weaker than that of the ADLM fAOD, with $\mathrm{ARF_{TOA}}$ and $\mathrm{ARF_{SFC}}$ differing by $>-30\ \mathrm{W/m^2}$. The atmospheric positive effect is also considerably less intense compared to the ADLM fAOD, with $\mathrm{ARF_{ATM}}$ differing by $>+20\ \mathrm{W/m^2}$.

■ DISCUSSION

GOSAT-2 is a dual-angle satellite instrument designed to capture the same scene from two different viewing angles simultaneously. It provides additional information about aerosol properties from the angular distribution of scattered light. We developed an ADLM to take advantage of the rich information to estimate fAOD. The model was applied to generate a new fAOD data set over the contiguous United States at a 460 m spatial resolution. Compared with using the traditional RF machine-learning model, there are fewer biases in ADLM-based fAODs, with the RMSE decreasing by 23% and more data falling within the EE (a relative improvement of 15%). Machine-learning models such as Random Forest (RF) lack inherent awareness of angular information, treating each input feature independently. This poses challenges in explicitly informing the model about the angular diversity of data, especially evident with dual-angle GOSAT-2 data, where aerosol properties measured at different angles exhibit strong interdependencies. Traditional models may overlook crucial angular information, resulting in biased estimations of the fine aerosol optical depth (fAOD). In contrast, the angle-dependent deep-learning model (ADLM) explicitly considers the angular diversity inherent in dual-angle observations, leveraging GOSAT-2's rich information to capture and model interdependencies among aerosol properties measured at different viewing angles. This enables ADLM to make more accurate fAOD estimations, surpassing the RF models. The validation and comparison results from ADLM underscore the superior performance achieved through our novel training data strategy, positioning it as a valuable and effective technique for improving the precision of fAOD retrievals. Additionally, the coarse spatial resolution fAOD product has long been criticized by researchers for its inability to accurately represent the complexities of fires, dust, and environmental structures on the Earth's surface.[63] Yet, the high spatial resolution of ADLM fAOD at 460 m equips us with the ability to gain deeper insight.

We found that the current MODIS, VIIRS, and MISR official products significantly underestimate wildfire-associated fAOD. Compared to AERONET, MODIS, VIIRS, and MISR underestimated fAOD by 47, 51, and 56%, respectively, during extreme wildfire events in California in September 2020. Particularly in daily fAOD monitoring, the underestimation of VIIRS results can reach 60% (Figure S6). This is a crucial factor contributing to our finding that fAOD ARF exhibits significantly greater cooling at the TOA and at the SFC and more warming within the ATM during active wildfire periods than what current VIIRS and MISR data indicate. Our estimates of atmospheric warming due to smoke using ALDM retrievals are considerably higher than those using MODIS, VIIRS, and MISR retrievals, with an increase in ARF_{ATM} of +15.6, + 31.2, and +43.9%, respectively. Furthermore, the cooling effect of wildfire fAOD at the TOA and at the SFC is significantly stronger than that represented by MODIS, VIIRS, and MISR fAODs, with both ARF_{TOA} and ARF_{SFC} increasing by approximately +20%. Zhao et al. have reported that once $|ARF_{SFC} - ARF_{ATM}|$ exceeds 55 W/m^2, the atmospheric-boundary-layer (ABL) structure tends to quickly stabilize.[64] Our results suggest that most $|ARF_{SFC} - ARF_{ATM}|$ values of wildfire fAOD are greater than 55 W/m^2, so a more stable ABL may be expected than what VIIRS and MISR fAOD estimates. This could provide useful information for relevant biomass-burning-environment model simulations.

■ ASSOCIATED CONTENT

Data Availability Statement

In this paper, the dual-angle images from GOSAT can be accessed at http://prdct.gosat-2.nies.go.jp/. The in situ measurements from AERONET and SURFRAD are available for download from https://aeronet.gsfc.nasa.gov and https://gml.noaa.gov/grad/surfrad/, respectively. The fire boundary data for California, sourced from FRAP, can be found at https://www.fire.ca.gov/what-we-do/fire-resource-assessment-program/fire-perimeters. Additionally, MODIS and VIIRS fAOD products are available at LAADS DAAC (https://ladsweb.modaps.eosdis.nasa.gov), while the MISR fAOD product can be obtained from https://asdc.larc.nasa.gov/project/MISR.

SI Supporting Information

The Supporting Information is available free of charge at https://pubs.acs.org/doi/10.1021/acs.est.4c02498.

> Evaluation metrics of ADLM (Section 1); CLAUDIA-3 cloud mask algorithm (Section 2); Ångström exponent interpolation (Section 3); model input variables (Section 4); main characteristics of the GOSAT-2 spacecraft (Table S1); main characteristics of the GOSAT-2/CAI-2 (Table S2); definition of different products for fAOD (Table S3); SURFRAD sites used for independent validation and their locations (Table S4); summary of ADLM model's input variables (Table S5); hyperparameters of the ADLM model settings (Table S6); AERONET and SURFRAD stations' spatial locations and data consistency comparison (Figure S1); ADLM model validation over in situ measurements and spatial performance (Figure S2); site-based 5-fold cross-validation of ADLM model (Figure S3); comparison of ADLM, ADLM-no-angle-fusion, and random forest fAOD estimates against AERONET (Figure S4); ADLM fAOD in an urban-scale emissions application (Figure S5); comparison of ADLM, VIIRS, MISR, and MODIS fAOD (Figure S6); monthly mean fAOD estimates and spatial performance in California and Montana (Figure S7); spatial details of fAOD chiefly caused by biomass combustion (Figure S8); fire perimeter data (FRAP) in California for the years 2019 to 2022 (Figure S9); mean fAOD radiative forcing from MODIS (Figure S10), VIIRS (Figure S11), and MISR (Figure S12) at the top of the atmosphere, within the atmosphere, and at the surface (PDF)

■ AUTHOR INFORMATION

Corresponding Author

Zhanqing Li − *Department of Atmospheric and Oceanic Science and ESSIC, University of Maryland, College Park, Maryland 20740, United States*; Email: zli@atmos.umd.edu

Authors

Xing Yan − *State Key Laboratory of Remote Sensing Science, Faculty of Geographical Science, Beijing Normal University, Beijing 100875, China*; orcid.org/0000-0001-9327-5756
Chen Zuo − *State Key Laboratory of Remote Sensing Science, Faculty of Geographical Science, Beijing Normal University, Beijing 100875, China*
Hans W. Chen − *Department of Space, Earth and Environment, Chalmers University of Technology, Gothenburg 41296, Sweden*; orcid.org/0000-0002-8601-6024
Yize Jiang − *State Key Laboratory of Remote Sensing Science, Faculty of Geographical Science, Beijing Normal University, Beijing 100875, China*
Qiao Wang − *Faculty of Geographical Science, Beijing Normal University, Beijing 100875, China*
Guoqiang Wang − *Faculty of Geographical Science, Beijing Normal University, Beijing 100875, China*
Kun Jia − *State Key Laboratory of Remote Sensing Science, Faculty of Geographical Science, Beijing Normal University, Beijing 100875, China*
Yinglan A − *Faculty of Geographical Science, Beijing Normal University, Beijing 100875, China*
Ziyue Chen − *State Key Laboratory of Remote Sensing Science, Faculty of Geographical Science, Beijing Normal University, Beijing 100875, China*
Jiayi Chen − *State Key Laboratory of Remote Sensing Science, Faculty of Geographical Science, Beijing Normal University, Beijing 100875, China*

Complete contact information is available at:
https://pubs.acs.org/10.1021/acs.est.4c02498

Author Contributions

X.Y. and Y.J. designed the research. C.Z. collected and analyzed the data. Z.L. supervised the project. X.Y. and C.Z. wrote the manuscript with support from H.W.C., Q.W, K.J., G.W., Y.A., Z.Y., and J.C. All authors discussed the results and contributed to the interpretation of final manuscript.

Notes

The authors declare no competing financial interest.

Code Availability The codes of ADLM are available online at https://github.com/Zc-1999/Angle-Dependent-Deep-Learning-Model-ADLM. And its user guide is at https://esidlm-tutorial.readthedocs.io/en/latest/quickstart/adlm_qs.html.

■ ACKNOWLEDGMENTS

This research has been supported by the National Natural Science Foundation of China (grant nos. 42030606 and 42192580), the Natural Science Foundation of Beijing (grant nos. 8222058), and the Fundamental Research Funds for the Central Universities. The authors gratefully acknowledge the European Centre for Medium Range Weather Forecasts, MODIS, MISR, VIIRS, SURFRAD, and AERONET teams for their effort in making the data available.

■ REFERENCES

(1) Liu, Z.; Ballantyne, A. P.; Cooper, L. A. Biophysical feedback of global forest fires on surface temperature. *Nat. Commun.* **2019**, *10* (1), No. 214.

(2) Abatzoglou, J. T.; Williams, A. P. Impact of anthropogenic climate change on wildfire across western US forests. *Proc. Natl. Acad. Sci. U.S.A.* **2016**, *113* (42), 11770−11775.

(3) Ramo, R.; Roteta, E.; Bistinas, I.; van Wees, D.; Bastarrika, A.; Chuvieco, E.; van der Werf, G. R. African burned area and fire carbon emissions are strongly impacted by small fires undetected by coarse resolution satellite data. *Proc. Natl. Acad. Sci. U.S.A.* **2021**, *118* (9), 1−7.

(4) Jolly, W. M.; Cochrane, M. A.; Freeborn, P. H.; Holden, Z. A.; Brown, T. J.; Williamson, G. J.; Bowman, D. M. J. S. Climate-induced variations in global wildfire danger from 1979 to 2013. *Nat. Commun.* **2015**, *6*, No. 7535.

(5) Zhang, L.; Lau, W.; Tao, W.; Li, Z. Large Wildfires in the Western United States Exacerbated by Tropospheric Drying Linked to a Multi-Decadal Trend in the Expansion of the Hadley Circulation. *Geophys. Res. Lett.* **2020**, *47* (16), e2020G−e87911G.

(6) Dennison, P. E.; Brewer, S. C.; Arnold, J. D.; Moritz, M. A. Large wildfire trends in the western United States, 1984−2011. *Geophys. Res. Lett.* **2014**, *41* (8), 2928−2933.

(7) McClure, C. D.; Jaffe, D. A. US particulate matter air quality improves except in wildfire-prone areas. *Proc. Natl. Acad. Sci. U.S.A.* **2018**, *115* (31), 7901−7906.

(8) Burke, M.; Childs, M. L.; de la Cuesta, B.; Qiu, M.; Li, J.; Gould, C. F.; Heft-Neal, S.; Wara, M. The contribution of wildfire to PM2.5 trends in the USA. *Nature* **2023**, *622* (622), 761.

(9) Bao, F.; Cheng, T.; Li, Y.; Gu, X.; Guo, H.; Wu, Y.; Wang, Y.; Gao, J. Retrieval of black carbon aerosol surface concentration using satellite remote sensing observations. *Remote Sens. Environ.* **2019**, *226*, 93−108.

(10) Li, C.; van Donkelaar, A.; Hammer, M. S.; McDuffie, E. E.; Burnett, R. T.; Spadaro, J. V.; Chatterjee, D.; Cohen, A. J.; Apte, J. S.; Southerland, V. A.; Anenberg, S. C.; Brauer, M.; Martin, R. V. Reversal of trends in global fine particulate matter air pollution. *Nat. Commun.* **2023**, *14* (1), No. 5349.

(11) Xu, R.; Ye, T.; Yue, X.; Yang, Z.; Yu, W.; Zhang, Y.; Bell, M. L.; Morawska, L.; Yu, P.; Zhang, Y.; Wu, Y.; Liu, Y.; Johnston, F.; Lei, Y.; Abramson, M. J.; Guo, Y.; Li, S. Global population exposure to landscape fire air pollution from 2000 to 2019. *Nature* **2023**, *621* (7979), 521−529.

(12) Gleason, K. E.; McConnell, J. R.; Arienzo, M. M.; Chellman, N.; Calvin, W. M. Four-fold increase in solar forcing on snow in western U.S. burned forests since 1999. *Nat. Commun.* **2019**, *10* (1), No. 2026.

(13) Bond, T. C.; Doherty, S. J.; Fahey, D. W.; Forster, P. M.; Berntsen, T.; DeAngelo, B. J.; Flanner, M. G.; Ghan, S.; Kärcher, B.; Koch, D.; Kinne, S.; Kondo, Y.; Quinn, P. K.; Sarofim, M. C.; Schultz, M. G.; Schulz, M.; Venkataraman, C.; Zhang, H.; Zhang, S.; Bellouin, N.; Guttikunda, S. K.; Hopke, P. K.; Jacobson, M. Z.; Kaiser, J. W.; Klimont, Z.; Lohmann, U.; Schwarz, J. P.; Shindell, D.; Storelvmo, T.; Warren, S. G.; Zender, C. S. Bounding the role of black carbon in the climate system: A scientific assessment. *J. Geophys. Res.: Atmos.* **2013**, *118* (11), 5380−5552.

(14) Bowman, D. M. J. S.; Williamson, G. J.; Abatzoglou, J. T.; Kolden, C. A.; Cochrane, M. A.; Smith, A. M. S. Human exposure and sensitivity to globally extreme wildfire events. *Nat. Ecol. Evol.* **2017**, *1* (3), 58.

(15) Yan, X.; Li, Z. Q.; Luo, N. N.; Shi, W. Z.; Zhao, W. J.; Yang, X. C.; Liang, C.; Zhang, F.; Cribb, M. An improved algorithm for retrieving the fine-mode fraction of aerosol optical thickness. Part 2: Application and validation in Asia. *Remote Sens. Environ.* **2019**, *222*, 90−103.

(16) Remer, L. A.; Kleidman, R. G.; Levy, R. C.; Kaufman, Y. J.; Tanré, D.; Mattoo, S.; Martins, J. V.; Ichoku, C.; Koren, I.; Yu, H.; Holben, B. N. Global aerosol climatology from the MODIS satellite sensors. *J. Geophys. Res.: Atmos.* **2008**, *113* (D14), D14S−D17S.

(17) Kaufman, Y. J.; Tanre, D.; Boucher, O. A satellite view of aerosols in the climate system. *Nature* **2002**, *419* (6903), 215−223.

(18) Zang, Z.; Li, D.; Guo, Y.; Shi, W.; Yan, X. Superior PM2.5 Estimation by Integrating Aerosol Fine Mode Data from the Himawari-8 Satellite in Deep and Classical Machine Learning Models. *Remote Sens.* **2021**, *13* (14), 2779.

(19) Zhu, J.; Xia, X.; Wang, J.; Che, H.; Chen, H.; Zhang, J.; Xu, X.; Levy, R.; Oo, M.; Holz, R.; Ayoub, M. Evaluation of Aerosol Optical Depth and Aerosol Models from VIIRS Retrieval Algorithms over North China Plain. *Remote Sens.* **2017**, *9* (5), 432.

(20) Gupta, P.; Levy, R. C.; Mattoo, S.; Remer, L. A.; Munchak, L. A. A surface reflectance scheme for retrieving aerosol optical depth over urban surfaces in MODIS dark target retrieval algorithm. *Atmos. Meas. Technol.* **2016**, *9* (9), 3293−3308.

(21) Bao, F.; Li, Y.; Gao, J. Carbonaceous aerosols remote sensing from geostationary satellite observation, Part I: Algorithm development using critical reflectance. *Remote Sens. Environ.* **2023**, *287*, No. 113459.

(22) Yang, L.; Ji, W.; Pei, X.; Si, Y.; Liu, H.; Chen, S.; Zhang, C.; Cheng, X.; Lu, X.; Wang, H. Global evaluation of Fengyun-3 MERSI dark target aerosol retrievals over land. *Int. J. Digit. Earth* **2024**, *17* (1), 1−24.

(23) Mielonen, T.; Levy, R. C.; Aaltonen, V.; Komppula, M.; de Leeuw, G.; Huttunen, J.; Lihavainen, H.; Kolmonen, P.; Lehtinen, K. E. J.; Arola, A. Evaluating the assumptions of surface reflectance and aerosol type selection within the MODIS aerosol retrieval over land: the problem of dust type selection. *Atmos. Meas. Technol.* **2011**, *4* (2), 201−214.

(24) Jethva, H.; Satheesh, S. K.; Srinivasan, J.; Levy, R. C. Improved retrieval of aerosol size-resolved properties from moderate resolution imaging spectroradiometer over India: Role of aerosol model and surface reflectance. *J. Geophys. Res.: Atmos.* **2010**, *115* (D18), No. D18213.

(25) Imasu, R.; Matsunaga, T.; Nakajima, M.; Yoshida, Y.; Shiomi, K.; Morino, I.; Saitoh, N.; Niwa, Y.; Someya, Y.; Oishi, Y.; Hashimoto, M.; Noda, H.; Hikosaka, K.; Uchino, O.; Maksyutov, S.; Takagi, H.; Ishida, H.; Nakajima, T. Y.; Nakajima, T.; Shi, C. Greenhouse gases Observing SATellite 2 (GOSAT-2): mission overview. *Prog. Earth Planet. Sci.* **2023**, *10* (1), 33−35.

(26) Sundström, A.-M.; Kolmonen, P.; Sogacheva, L.; de Leeuw, G. Aerosol retrievals over China with the AATSR dual view algorithm. *Remote Sens. Environ.* **2012**, *116*, 189−198.

(27) Guang, J.; Xue, Y.; Wang, Y.; Li, Y.; Mei, L.; Xu, H.; Liang, S.; Wang, J.; Bai, L. Simultaneous determination of aerosol optical thickness and surface reflectance using ASTER visible to near-infrared data over land. *Int. J. Remote Sens.* **2011**, *32* (22), 6961−6974.

(28) Limbacher, J. A.; Kahn, R. A.; Lee, J. The new MISR research aerosol retrieval algorithm: a multi-angle, multi-spectral, bounded-variable least squares retrieval of aerosol particle properties over both land and water. *Atmos. Meas. Technol.* **2022**, *15* (22), 6865−6887.

(29) Kahn, R. A.; Gaitley, B. J. An analysis of global aerosol type as retrieved by MISR. *J. Geophys. Res.: Atmos.* **2015**, *120* (9), 4248−4281.

(30) Amini, S.; Momeni, M.; Monadjemi, A. Sensitivity analysis of Look-up table for satellite-based aerosol optical depth retrieval. *J. Aerosol Sci.* **2021**, *158*, No. 105842.

(31) Shi, C.; Hashimoto, M.; Shiomi, K.; Nakajima, T. Development of an Algorithm to Retrieve Aerosol Optical Properties Over Water Using an Artificial Neural Network Radiative Transfer Scheme: First Result From GOSAT-2/CAI-2. *IEEE Trans. Geosci. Remote Sens.* **2021**, *59* (12), 9861−9872.

(32) Su, X.; Wang, L.; Gui, X.; Yang, L.; Li, L.; Zhang, M.; Qin, W.; Tao, M.; Wang, S.; Wang, L. Retrieval of total and fine mode aerosol optical depth by an improved MODIS Dark Target algorithm. *Environ. Int.* **2022**, *166*, No. 107343.

(33) Yang, L.; Xue, Y.; Guang, J.; Kazemian, H.; Zhang, J.; Li, C. Improved Aerosol Optical Depth and Ångstrom Exponent Retrieval Over Land From MODIS Based on the Non-Lambertian Forward Model. *IEEE Geosci. Remote Sens. Lett.* **2014**, *11* (9), 1629−1633.

(34) Lee, C. S.; Yeom, J. M.; Lee, H. L.; Kim, J.; Han, K. Sensitivity analysis of 6S-based look-up table for surface reflectance retrieval. *Asia-Pac. J. Atmos. Sci.* **2015**, *51* (1), 91−101.

(35) Chen, X.; de Leeuw, G.; Arola, A.; Liu, S.; Liu, Y.; Li, Z.; Zhang, K. Joint retrieval of the aerosol fine mode fraction and optical depth using MODIS spectral reflectance over northern and eastern China: Artificial neural network method. *Remote Sens. Environ.* **2020**, *249*, No. 112006.

(36) Kang, Y.; Kim, M.; Kang, E.; Cho, D.; Im, J. Improved retrievals of aerosol optical depth and fine mode fraction from GOCI geostationary satellite data using machine learning over East Asia. *ISPRS J. Photogramm. Remote Sens.* **2022**, *183*, 253−268.

(37) Liang, C.; Zang, Z.; Li, Z.; Yan, X. An Improved Global Land Anthropogenic Aerosol Product Based on Satellite Retrievals From 2008 to 2016. *IEEE Geosci. Remote Sens. Lett.* **2021**, *18* (6), 944−948.

(38) Yan, X.; Zang, Z.; Jiang, Y. Z.; Shi, W. Z.; Guo, Y. S.; Li, D.; Zhao, C. F.; Husi, L. T. A Spatial-Temporal Interpretable Deep Learning Model for improving interpretability and predictive accuracy of satellite-based PM2.5. *Environ. Pollut.* **2021**, *273*, No. 116459.

(39) Yan, X.; Zang, Z.; Liang, C.; Luo, N. N.; Ren, R. M.; Cribb, M.; Li, Z. Q. New global aerosol fine-mode fraction data over land derived from MODIS satellite retrievals. *Environ. Pollut.* **2021**, *276* (276), No. 116707.

(40) Yan, X.; Zang, Z.; Luo, N. N.; Jiang, Y. Z.; Li, Z. Q. New interpretable deep learning model to monitor real-time PM2.5 concentrations from satellite data. *Environ. Int.* **2020**, *144*, No. 106060, DOI: 10.1016/j.envint.2020.106060.

(41) Li, T.; Yang, Q.; Wang, Y.; Wu, J. Joint estimation of PM2.5 and O3 over China using a knowledge-informed neural network. *Geosci. Front.* **2023**, *14* (2), 282−294.

(42) Ishida, H.; Oishi, Y.; Morita, K.; Moriwaki, K.; Nakajima, T. Y. Development of a support vector machine based cloud detection method for MODIS with the adjustability to various conditions. *Remote Sens. Environ.* **2018**, *205*, 390−407.

(43) Oishi, Y.; Ishida, H.; Nakajima, T. Y.; Nakamura, R.; Matsunaga, T. Preliminary verification for application of a support vector machine-based cloud detection method to GOSAT-2 CAI-2. *Atmos. Meas. Technol.* **2018**, *11* (5), 2863−2878.

(44) Wolfe, R. E.; Lin, G.; Nishihama, M.; Tewari, K. P.; Tilton, J. C.; Isaacman, A. R. Suomi NPP VIIRS prelaunch and on-orbit geometric calibration and characterization. *J. Geophys. Res.: Atmos.* **2013**, *118* (20), 11.

(45) Povey, A. C.; Grainger, R. G. Toward More Representative Gridded Satellite Products. *IEEE Geosci. Remote Sens. Lett.* **2019**, *16* (5), 672−676.

(46) Garay, M. J.; Witek, M. L.; Kahn, R. A.; Seidel, F. C.; Limbacher, J. A.; Bull, M. A.; Diner, D. J.; Hansen, E. G.; Kalashnikova, O. V.; Lee, H.; Nastan, A. M.; Yu, Y. Introducing the 4.4 km spatial resolution Multi-Angle Imaging SpectroRadiometer (MISR) aerosol product. *Atmos. Meas. Technol.* **2020**, *13* (2), 593−628.

(47) Holben, B. N.; Eck, T. F.; Slutsker, I.; Tanre, D.; Buis, J. P.; Setzer, A.; Vermote, E.; Reagan, J. A.; Kaufman, Y. J.; Nakajima, T.; Lavenu, F.; Jankowiak, I.; Smirnov, A. AERONET—A federated instrument network and data archive for aerosol characterization. *Remote Sens. Environ.* **1998**, *66* (1), 1−16.

(48) Yan, X.; Li, Z. Q.; Shi, W. Z.; Luo, N. N.; Wu, T. X.; Zhao, W. J. An improved algorithm for retrieving the fine-mode fraction of aerosol optical thickness, part 1: Algorithm development. *Remote Sens. Environ.* **2017**, *192*, 87−97.

(49) Augustine, J. A.; Hodges, G. B.; Cornwall, C. R.; Michalsky, J. J.; Medina, C. I. An Update on SURFRAD—The GCOS Surface Radiation Budget Network for the Continental United States. *J. Atmos. Ocean. Technol.* **2005**, *22* (10), 1460−1472.

(50) Wang, L.; Yisen, C.; Ying, N.; Salazar, G. A.; Wei, G. Analysis of atmospheric turbidity in clear skies at Wuhan, Central China. *J. Earth Sci.* **2017**, *28* (4), 729−738.

(51) Wang, L.; Gong, W.; Xia, X.; Zhu, J.; Li, J.; Zhu, Z. Long-term observations of aerosol optical properties at Wuhan, an urban site in Central China. *Atmos. Environ.* **2015**, *101*, 94−102.

(52) Syphard, A. D.; Keeley, J. E. Historical reconstructions of California wildfires vary by data source. *Int. J. Wildland Fire.* **2016**, *25* (12), 1221−1227.

(53) Masri, S.; Scaduto, E.; Jin, Y.; Wu, J. Disproportionate Impacts of Wildfires among Elderly and Low-Income Communities in California from 2000 to 2020. *Int. J. Environ. Res. Public Health* **2021**, *18* (8), 3921.

(54) Butry, D. T.; Thomas, D. S. Underreporting of wildland fires in the US Fire Reporting System NFIRS: California. *Int. J. Wildland Fire* **2017**, *26* (8), 732.

(55) Vaswani, A.; Shazeer, N.; Parmar, N.; Uszkoreit, J.; Jones, L.; Gomez, A. N.; Kaiser, L.; Polosukhin, I. Presented in Part at the Advances in Neural Information Processing Systems 30 (NIPS 2017), 2017.

(56) Gorishniy, Y.; Rubachev, I.; Khrulkov, V.; Babenko, A. Presented in Part at the 35th Conference on Neural Information Processing Systems (NeurIPS), 2021.

(57) Nakajima, T.; Sekiguchi, M.; Okada, I.; Takamura, T.; Kawamoto, K.; Takemura, T.; Uno, I.; Higurashi, A.; Kim, D.; Sohn, B. J.; Oh, S.; Nakajima, T. Y.; Ohta, S. Significance of direct and indirect radiative forcings of aerosols in the East China Sea region: Characterization of Asian aerosols and their radiative impacts on climate. *J. Geophys. Res.: Atmos.* **2003**, *108* (D23), E21−E26.

(58) Kumar, K. R.; Yin, Y.; Sivakumar, V.; Kang, N.; Yu, X.; Diao, Y.; Adesina, A. J.; Reddy, R. R. Aerosol climatology and discrimination of aerosol types retrieved from MODIS, MISR and OMI over Durban (29.88°S, 31.02°E), South Africa. *Atmos. Environ.* **2015**, *117*, 9−18.

(59) Ramo, R.; Roteta, E.; Bistinas, I.; van Wees, D.; Bastarrika, A.; Chuvieco, E.; van der Werf, G. R. African burned area and fire carbon emissions are strongly impacted by small fires undetected by coarse resolution satellite data. *Proc. Natl. Acad. Sci. U.S.A.* **2021**, *118* (9), No. e2011160118.

(60) Wu, L.; Su, H.; Jiang, J. H. Regional simulations of deep convection and biomass burning over South America: 2. Biomass burning aerosol effects on clouds and precipitation. *J. Geophys. Res.: Atmos.* **2011**, *116* (D17), No. D17209.

(61) Liu, L.; Cheng, Y.; Wang, S.; Wei, C.; Pohlker, M. L.; Pohlker, C.; Artaxo, P.; Shrivastava, M.; Andreae, M. O.; Poschl, U.; Su, H.; Pacific Northwest National Laboratory PNNL, R.W.U.S.. Impact of biomass burning aerosols on radiation, clouds, and precipitation over the Amazon: relative importance of aerosol−cloud and aerosol−radiation interactions. *Atmos. Chem. Phys.* **2020**, *20* (21), 13283−13301.

(62) Chemke, R.; Dagan, G. The Effects of the Spatial Distribution of Direct Anthropogenic Aerosols Radiative Forcing on Atmospheric Circulation. *J. Clim.* **2018**, *31* (17), 7129−7145.

(63) Yu, Y.; Ginoux, P. Enhanced dust emission following large wildfires due to vegetation disturbance. *Nat. Geosci.* **2022**, *15* (11), 878−884.

(64) Zhao, D.; Xin, J.; Gong, C.; Quan, J.; Wang, Y.; Tang, G.; Ma, Y.; Dai, L.; Wu, X.; Liu, G.; Ma, Y. The impact threshold of the aerosol radiative forcing on the boundary layer structure in the pollution region. *Atmos. Chem. Phys.* **2021**, *21* (7), 5739−5753.